Winter February 28, 2014

Physical processes at work in sub-30fs, PW laser pulse-driven plasma accelerators: Towards GeV electron acceleration experiments at CILEX facility.

Arnaud Beck
Serge Y. Kalmykov
Xavier Davoine
Agustin F. Lifschitz
Bradley A. Shadwick, et al.

Nuclear Instruments and Methods in Physics Research A 740 (2014) 67–73

Contents lists available at ScienceDirect

Nuclear Instruments and Methods in Physics Research A

journal homepage: www.elsevier.com/locate/nima

Physical processes at work in sub-30 fs, PW laser pulse-driven plasma accelerators: Towards GeV electron acceleration experiments at CILEX facility

A. Beck [a,*], S.Y. Kalmykov [b], X. Davoine [d], A. Lifschitz [c], B.A. Shadwick [b], V. Malka [c], A. Specka [a]

[a] Laboratoire Leprince-Ringuet – École Polytechnique, CNRS-IN2P3, Palaiseau 91128, France
[b] Department of Physics and Astronomy, University of Nebraska – Lincoln, Nebraska 68588-0299, USA
[c] Laboratoire d'Optique Appliquée, ENSTA ParisTech-CNRS UMR7639-École Polytechnique, Palaiseau 91762, France
[d] CEA, DAM, DIF, Arpajon F-91297, France

ARTICLE INFO

Available online 11 November 2013

Keywords:
Laser wakefield acceleration
Petawatt laser
Blowout regime
Electron self-injection
Optical shock
Particle-in-cell simulations

ABSTRACT

Optimal regimes and physical processes at work are identified for the first round of laser wakefield acceleration experiments proposed at a future CILEX facility. The Apollon-10P CILEX laser, delivering fully compressed, near-PW-power pulses of sub-25 fs duration, is well suited for driving electron density wakes in the blowout regime in cm-length gas targets. Early destruction of the pulse (partly due to energy depletion) prevents electrons from reaching dephasing, limiting the energy gain to about 3 GeV. However, the optimal operating regimes, found with reduced and full three-dimensional particle-in-cell simulations, show high energy efficiency, with about 10% of incident pulse energy transferred to 3 GeV electron bunches with sub-5% energy spread, half-nC charge, and absolutely no low-energy background. This optimal acceleration occurs in 2 cm length plasmas of electron density below $10^{18}\ \mathrm{cm}^{-3}$. Due to their high charge and low phase space volume, these multi-GeV bunches are tailor-made for staged acceleration planned in the framework of the CILEX project. The hallmarks of the optimal regime are electron self-injection at the early stage of laser pulse propagation, stable self-guiding of the pulse through the entire acceleration process, and no need for an external plasma channel. With the initial focal spot closely matched for the nonlinear self-guiding, the laser pulse stabilizes transversely within two Rayleigh lengths, preventing subsequent evolution of the accelerating bucket. This dynamics prevents continuous self-injection of background electrons, preserving low phase space volume of the bunch through the plasma. Near the end of propagation, an optical shock builds up in the pulse tail. This neither disrupts pulse propagation nor produces any noticeable low-energy background in the electron spectra, which is in striking contrast with most of existing GeV-scale acceleration experiments.

1. Introduction

Acceleration of electrons in laser-driven plasma wakes has been the focus of keen interest over the last three decades. The introduction of laser facilities delivering 100-terawatt (TW)-class mid-IR pulses at high repetition rates greatly advanced this area. With such lasers, it became possible to achieve a complete ponderomotive blowout of the electron fluid in low-density plasmas (keeping the much heavier ions at rest), maintaining the cavity ("bubble") of electron density over many Rayleigh lengths. The resulting extension of the acceleration length to the centimeter range, combined with a GeV/cm-scale gradient supported by the bubble, culminated in production of low phase-space-volume electron bunches with energies close to 1 GeV [1–3]. A sea change in the field of laser plasma acceleration (LPA) should come with the further progress in laser technology. The state-of-art systems are presently delivering short (15–30 fs) petawatt (PW) laser pulses with 0.1–10 Hz repetition rate [3–6]. Per standard LPA scalings [7], experiments at these facilities promise boosting electron energy to a few GeV, producing beams with parameters competitive with the standard linacs, but with the flexibility in parameters not easily afforded by the standard accelerator technology.

The future CILEX (Centre Interdisciplinaire de la Lumiere EXtrême/Interdisciplinary Center for the Extreme Light) is one facility of this kind that targets diverse applications using plasmas produced by 1–10 PW, short-pulse lasers. It will host the Apollon-10P laser, which will deliver pulses with an instantaneous power up to 10 PW, and the associated infrastructure and experimental setups. It will thus offer an opportunity of scientific breakthroughs in various domains [8]. The facility is located in France (Paris area) and is expected to open to the international user community around 2015.

* Corresponding author. Tel.: +33 169335593.
E-mail addresses: beck@llr.in2p3.fr (A. Beck), skalmykov2@unl.edu (S.Y. Kalmykov).

0168-9002/$ - see front matter © 2013 Elsevier B.V. All rights reserved.
http://dx.doi.org/10.1016/j.nima.2013.11.003

The LPA is at the core of the CILEX scientific program, with the first and foremost task to explore the experimental prospects of using ultrashort PW pulses for multi-GeV acceleration. Starting with a pulse duration of $\tau_L \approx 25$ fs (FWHM in intensity) in preparation for even shorter pulses, the first shots are expected to have the pulse energy on target between 15 and 25 J (0.6–1 PW power). The carrier wavelength of the Apollon-10P laser is $\lambda_0 = 0.8$ μm. A 30 μm−radius focal spot, yielding 4–6.6 × 10^{19} W/cm^2 intensity on target, can be easily afforded by the laboratory design constraints. Using these parameters, we give a comprehensive analysis of the laser plasma interaction, including the associated relativistic optical phenomena. We focus on acceleration beyond 1 GeV, exploring the regimes that maximize the electron energy without beam quality degradation. A very basic configuration will be implemented in the first round of experiments. The acceleration will occur in the blowout regime, taking advantage of electron self-injection and laser pulse self-guiding (over a few Rayleigh lengths) in a low-pressure gas/plasma cell. The results of three-dimensional particle-in-cell (3D PIC) simulations reported here show that few-GeV electron bunches can be produced with a low phase space volume and high enough charge to be used for either radiation physics applications or staged acceleration; both applications are the top priorities on the CILEX agenda [8].

With the laser parameters prescribed by the amplifier and focusing system, the acceleration process can be optimized by changing the pressure (density) in the gas cell and the cell length [9–11]. This way, electron bunches with charge of a few hundred pC, tunable in energy up to 3 GeV, having less than 5% root-mean-square (RMS) energy spread (no low-energy tail), can be produced from 1–2 cm length plasmas of density less than 10^{18} cm^{-3}. In Section 2 we give parameters for background-free GeV acceleration considering the requirements for stable self-guided pulse propagation. These arguments are supported by extensive parameter scans using quasistatic PIC simulations with the axi-symmetric code WAKE [12–14] with test particle tracking [9–11,15,16]. Section 3 provides detailed PIC simulations for the optimal set of parameters taken from the center of the range defined in Section 2. Section 3.1 uses the results of WAKE simulation to identify the nonlinear optical processes at work and explain the details of pulse evolution for acceleration beyond the theoretical pulse depletion limit. It is found that the optimal choice of parameters stabilizes the transverse evolution of the pulse after a brief transient period. The electron density bubble, evolving in lock-step with the optical driver, self-injects electrons early, and then remains almost frozen, completely suppressing further injection. The quasi-monoenergetic (QME) electron bunch thus stays background-free throughout the entire acceleration process. In addition, frequency red-shifting of the laser pulse due to wake excitation causes longitudinal deformations of the pulse (self-compression and formation of the optical shock). These deformations have the same physical nature as in high-density regimes of LPA [15–17], but manifest in a much less disruptive fashion. Modest frequency red-shifting and incomplete electron cavitation avoid the intensity build-up in the pulse front and formation of a steep rising edge. Instead, the optical shock forms in the pulse tail area at the end of the propagation, and the slowly-rising, low-amplitude leading edge diffracts freely [18–20]. These deformations reduce the efficiency of wake excitation, terminating the acceleration process, but otherwise do not degrade the electron beam quality. Presented in Section 3.2 results of fully explicit 3D PIC simulations using CALDER-Circ code [21] confirm this evolution scenario, demonstrating background-free acceleration to 2.85 GeV. Section 4 outlines the results and points out the directions of future work.

2. Parameter space for background-free GeV acceleration

The fundamental physical process underlying the operation of the CILEX accelerator is the balance between the relativistic and ponderomotive effects in laser pulse self-focusing. The relativistic mass effect increases the nonlinear index of refraction near the axis, compensating for linear diffraction, potentially leading to the pulse focusing once the pulse power exceeds the threshold $P_{\rm cr} = 16\gamma_{\rm g}^2$ GW [22]. Here, $\gamma_{\rm g} = \omega_0/\omega_{\rm p} \gg 1$ is the Lorentz factor associated with the linear group velocity of the pulse in plasma, $\omega_0 = 2\pi c/\lambda_0$ is the pulse carrier frequency, $\omega_{\rm p} = (4\pi e^2 n_0/m_e)^{1/2}$ is the plasma frequency, $-|e|$ is the electron charge, m_e is the electron rest mass, and n_0 is the background electron plasma density. Radiation pressure compresses the electron fluid, increasing the electron density at the pulse leading edge, thus locally reducing the nonlinear index. Once the pulse is shorter than $\omega_{\rm p}^{-1}$, relativistic and ponderomotive contributions to the index tend to cancel out each other. The pulse then diffracts as under vacuum even though its power may exceed the critical power by an order of magnitude [23–25].

Tipping the balance between the two effects in favor of relativistic self-focusing occurs when $\omega_{\rm p}\tau_L \geq 1$, which sets the lower limit of electron density,

$$n_0 \geq n_- = 3.144 \times 10^{20} (\tau_L[\text{fs}])^{-2}\ \text{cm}^{-3}. \tag{1}$$

Under the condition $n_0 \approx n_-$, the uncompensated relativistic self-focusing inhibits the diffraction [25,26] if

$$P \geq 10 P_{\rm cr} \equiv P_- = 2.835 \times 10^{17} (n_0[\text{cm}^{-3}])^{-1}\ \text{PW}. \tag{2}$$

Electron energy gain in the regime $n_0 \approx n_-$ can be estimated from the following considerations. At the plasma entrance, the pulse is sufficiently intense to produce a bubble that rapidly expands and self-injects an electron bunch. As the pulse diffracts, the bubble turns into the first period of the nonlinear plasma wave. Injection thus stops and never resumes, whereas phase space rotation reduces the beam energy spread to a few-percent level [9–11, 15,16]. The first wake period contracts as the wave amplitude drops [25,26], releasing the accelerated electrons after a propagation over a couple of Rayleigh lengths. This sets the effective acceleration length $L_{\rm acc}^- \approx 2z_R = (2\pi/\lambda_0) r_0^2$, where r_0 is the laser beam waist at $\exp(-2)$ of the peak intensity. As the pulse diffracts, the wake amplitude remains close to the maximum amplitude accessible in the blowout regime [7]. This yields the energy gain

$$\mathcal{E}_- = 2z_R E_{\rm acc}^- \approx 2^{3/2} (P/P_{\rm cr})^{1/6} (m_e \omega_{\rm p} c/|e|) z_R.$$

The choice of the laser waist, $r_0 = 30$ μm, yields merely 0.7 cm acceleration length in the diffraction-limited regime. There are two ways to extend the pulse propagation length and increase the energy gain. One is to enforce the relativistic self-focusing by raising the laser power, and the other is to increase the plasma density. Raising the power suppresses diffraction, but going beyond $P = 25P_{\rm cr}$ seems unreasonable. WAKE simulations indicate that, at this high power ratio, the pulse spot and intensity start oscillating before the stable self-guiding sets in. The resulting periodic self-injection degrades the electron bunch spectrum [9]. The upper limit on the laser power is thus

$$P \leq 25 P_{\rm cr} \equiv P_+ = 7.1 \times 10^{17} (n_0[\text{cm}^{-3}])^{-1}\ \text{PW}. \tag{3}$$

Increasing the density also enhances relativistic self-focusing, eventually leading to self-channeling with almost complete electron cavitation [7,12]. In this regime, the pulse propagation and electron acceleration are limited by the pulse depletion, which yields $L_{\rm acc}^+ \approx c\tau_L \gamma_{\rm g}^2$ [7]. The acceleration length thus increases by a factor

$$\Delta L_{\rm acc} = L_{\rm acc}^+ / L_{\rm acc}^- = 2\pi (c\tau_L/\lambda_0)(\omega_{\rm p} r_0/c)^{-2}.$$

Because of rapid pulse depletion, self-injected electrons remain far from dephasing, staying close to the peak of accelerating gradient, $E_{\rm acc}^+ \approx 2^{1/2} (P/P_{\rm cr})^{1/6} (m_e \omega_{\rm p} c/|e|)$. This results in an energy-efficient

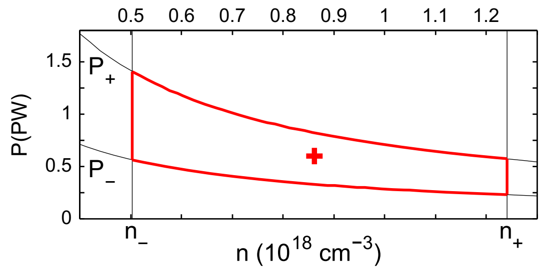

Fig. 1. Parameter space for the background-free, GeV LPA with a 25 fs pulse [the area delimited with red (gray) curves]. The lower density limit, n_-, corresponds to the diffraction-limited propagation ($\omega_p^- \tau_L = 1$); n_+ corresponds to the depletion-limited propagation without catastrophic self-focusing ($\omega_p^+ \tau_L = \pi/2$). The lower power limit, $P_- = 10P_{cr}$, corresponds to diffraction-limited propagation; the upper limit, $P_+ = 25P_{cr}$, corresponds to the self-channeled, depletion-limited propagation with minimized oscillations of the laser spot size. The cross marks the parameters of the optimal regime studied in detail in Section 3. Figs. 2–7 correspond to this regime.

acceleration process (cf. Section 3.2) with the energy gain

$\mathcal{E}_+ \approx 2^{1/2}(P/P_{cr})^{1/6}\gamma_g^2(m_e\omega_p c/|e|)c\tau_L$.

This gain, however, scales as $\mathcal{E}[\text{GeV}] \approx 1.3 \times 10^5 (n_0[\text{cm}^{-3}])^{-1/3} \times (P[\text{PW}])^{1/6}\tau_L[\text{fs}]$. Therefore, increasing density too much reduces the efficiency. And, as P approaches P_+, transient oscillations the laser spot and intensity degrade electron beam quality. Parameter scans using WAKE simulations indicate that for $P_- \le P \le P_+$ and $\omega_p\tau_L = \pi/2$ the pulse propagation is not yet compromised. This sets the upper limit on density:

$$n_0 \le n_+ \equiv (\pi/2)^2 n_- = 7.76 \times 10^{20} (\tau_L[\text{fs}])^{-2}\ \text{cm}^{-3} \tag{4}$$

Fig. 1 shows the parameter space defined by Eqs. (1)–(4) for the 25 fs-length pulse. Its lower-left corner, $n_- = 5 \times 10^{17}$ cm^{-2} and $P_- =$ 0.56 PW, yields $L_{acc}^- \approx 0.7$ cm, $E_{acc}^- \approx 1.4$ GV/cm, and $\mathcal{E}_- \approx$ 1 GeV. The upper-right corner, $n_+ \approx 1.24 \times 10^{18}$ cm^{-3} and $P_+ \approx 0.57$ PW, yields $L_{acc}^+ \approx 1.06$ cm, $E_{acc}^+ \approx 2.6$ GV/cm, and $\mathcal{E}_+ \approx 2.75$ GeV. WAKE simulations with test particles and CALDER-Circ simulations corroborate these estimates within a 15% margin of agreement.

The important point to be made is that as the laser power grows, the density window for the background-free acceleration closes very rapidly. For P=0.6 PW, almost the entire range $n_- \le n_0 \le n_+$ is available, whereas for $P \approx 1$ PW the upper density limit reduces to $n_0 \approx 7 \times 10^{17}$ cm^{-3}, narrowing the density window by a factor of 3.5. Further, there is practically no freedom in accelerator parameters for $P \approx 1.5$ PW. This is not surprising; for PW pulses as short as $\omega_p\tau_L \sim 1$, the balance between vacuum-like diffraction and catastrophic self-focusing critically depends on a few-percent variation of power and density, reducing our ability to control the acceleration process and the final parameters of electron beams.

3. Physical processes at work in the optimal regime: Back-ground-free 2.85 GeV electron bunch from 2 cm plasma

To explore in detail the physical processes at work in the optimal acceleration regime, we select the parameters from the center of the window in Fig. 1. With these parameters, our reduced and full 3D PIC simulations reproduce all the hallmarks of the regime: (1) relativistic self-focusing of the pulse sufficient to create the ponderomotive blowout (the bubble); (2) transient evolution of the system sufficient to cause self-injection of ambient plasma electrons; (3) rapid termination of self-injection and formation of a QME electron bunch; (4) acceleration of this bunch to a few-GeV energy over at least 1 cm distance, with identically zero low-energy background.

The laser pulse and plasma parameters are as follows. The plasma begins at x=0 and has a 0.5 mm-length entrance ramp followed by a flat portion with the density $n_0 = 8.62 \times 10^{17}$ cm^{-3}. The pulse is focused at the foot of the ramp and propagates toward positive x. The pulse carrier wavelength, $\lambda_0 = 0.8$ μm, corresponds to $\gamma_g \approx 45$. The amplitude of normalized vector potential is given by $a(x=0) = a_0 \exp[-(r/r_0)^2 - 2\ln 2\xi^2/(c\tau_L)^2]$, where $\xi = ct - x$, $r = (y^2+z^2)^{1/2}$, $\tau_L = 25$ fs ($\omega_p\tau_L = 1.31$), $r_0 = 30$ μm ($\omega_p r_0/c = 5.24$), and a_0=4.3. The latter yields the peak intensity at focus $I_0 = 4 \times 10^{19}$ W/cm^2, average power P=0.6 PW, and $P/P_{cr} \approx 18$. The pulse spot is 15% wider than the matched size, $r_m = (c/\omega_p)2^{3/2}(P/P_{cr})^{1/6} \approx 26$ μm. Even though the pulse depletion length, $L_d \approx c\tau_L\gamma_g^2$, is only 1.5 cm, we run the simulations through $x \approx 2$ cm (or $5.7z_R$) to find details of pulse and electron bunch beyond the theoretical depletion limit. Details of the laser pulse evolution and self-injection process presented in Figs. 2–7 correspond to this set of parameters.

3.1. Evolution of optical driver

The cylindrically symmetric, time-averaged (over ω_0^{-1}) quasi-static PIC code WAKE [12] computes the complex envelope of the laser vector potential using an extended paraxial solver. To preserve group velocity dispersion (GVD) over a broad frequency range and to calculate precisely radiation absorption due to wake excitation in the situation with large frequency shifts [13,14], we use the longitudinal grid $\Delta\xi \approx \lambda_0/4 \approx 0.2$ μm. The radial grid is three times coarser. We use 30 particles per radial cell and the time step $\omega_0\Delta t \approx 10.125$. Under these conditions, WAKE correctly captures all relevant physics of pulse propagation and evolution of the bubble [9–11].

The envelope code WAKE is perfectly suited for studying the nonlinear optical evolution of the driver, with the focus on spectral modifications and amplitude distortion caused by the wake excitation [13,14]. Variation of the pulse integral characteristics and peak amplitude in the course of propagation is shown in Fig. 2. The integral characteristics are the energy [Fig. 2(a)]; radially integrated mean frequency and frequency variance [Figs. 2(b) and (c), respectively],

$$\langle\omega(x)\rangle = \frac{\omega_0}{W^2(x)}\int_0^\infty r\,dr\int_0^\infty \omega|a(x,r,\omega)|^2\,d\omega \tag{5}$$

$$\langle\Delta\omega(x)\rangle^2 = \frac{1}{W^2(x)}\int_0^\infty r\,dr\int_0^\infty (\omega-\langle\omega\rangle)^2|a(x,r,\omega)|^2\,d\omega \tag{6}$$

where $a(x,r,\omega) = \int_{-\infty}^{+\infty} a(x,r,\xi)\exp[-i(\omega_0-\omega)\xi/c]\,d\xi/c$ is the Fourier transform, and $W^2(x) = \omega_0^2\int_0^\infty r\,dr\int_0^\infty |a(x,r,\omega)|^2\,d\omega$; and the mean pulse length computed as a ξ-variance of the energy density on axis [Fig. 2(d)],

$$\langle\Delta\tau(x)\rangle^2 = \frac{8\ln 2}{U^2(x)}\int_{-\infty}^\infty (\xi - c\langle\tau\rangle)^2|a(x,0,\xi)|^2\,d\xi \tag{7}$$

where $\langle\tau\rangle = cU^{-2}\int_{-\infty}^\infty \xi|a(x,0,\xi)|^2\,d\xi$ is the position of the beam centroid, and $U^2(x) = c^2\int_{-\infty}^\infty |a(x,0,\xi)|^2\,d\xi$. Snapshots of the pulse amplitude $|a(x,r,\xi)|$ are shown in Fig. 3 near the points of the strongest transverse and longitudinal compression [panels (a) and (b), respectively], and through the process of optical shock formation [panels (c) and (d)]. Fig. 4 links longitudinal distortion of the pulse [cf. axial lineouts of normalized intensity in panels (a.1)–(d.1), which correspond to the amplitude snapshots in Fig. 3(a)–(d)] to the local frequency shift on axis [panels (a.2)–(d.2)]. This shift is extracted from the complex envelope of the vector potential, $a(x,0,\xi) = |a|\exp(i\phi)$, using two independent methods. First, the Wigner transform of the envelope, $\mathcal{W}(x,\xi,\omega) = (2\pi c)^{-1}\int_{-\infty}^{+\infty} a(x,\xi+(\xi'/2))a^*(x,\xi-(\xi'/2))$ $\exp[-i(\omega_0-\omega)\xi'/c]\,d\xi'$ yields the distribution of "photon density" in the "photon phase space," (ξ,ω). Secondly, we calculate the "instantaneous" frequency as the rate of the envelope phase change,

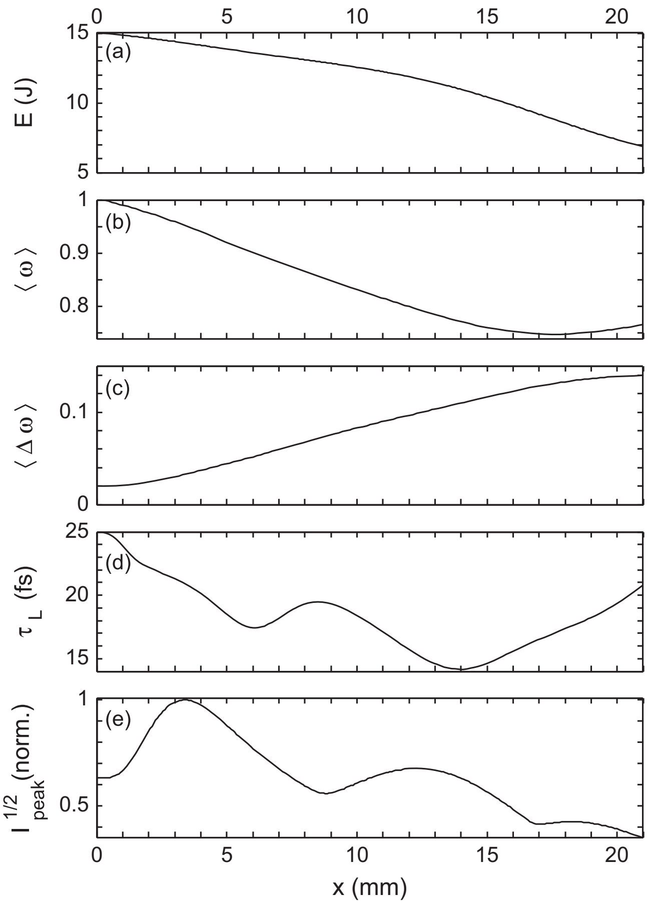

Fig. 2. Evolution of the laser pulse parameters in the course of pulse propagation. The pulse propagates from left to right. (a) Laser pulse energy, (b) mean frequency (in units of ω_0), (c) frequency bandwidth (in units of ω_0), (d) pulse length computed from the ξ-variance of the energy density on axis, (e) normalized peak amplitude of the pulse vector potential. (WAKE simulation.)

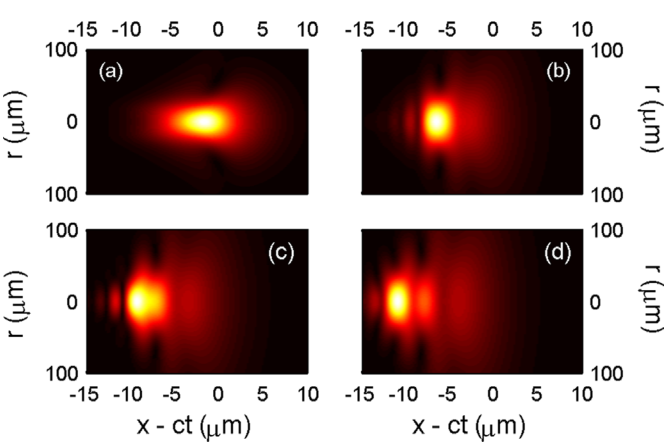

Fig. 3. Snapshots of the laser vector potential $|a(r,\xi)|$ at (a) $x=0.6$ cm, (b) 1.45 cm, (c) 1.8 cm, and (d) 2.1 cm. The pulse propagates from left to right. The amplitude is normalized to its peak value in each snapshot; the linear color map spans from 0 to 1. The strongest pulse compression occurs at $x=1.45$ cm [cf. Fig. 2(e)], at which point formation of the optical shock begins in the tail [cf. panels (b)–(d)]. As red-shifted radiation slides through the pulse, building up the shock, the RMS pulse length grows [cf. Fig. 2(e)], and the low-amplitude, slowly rising front diffracts. (WAKE simulation).

$\omega(\xi)=\omega_0-\mathrm{d}\phi/\mathrm{d}t=\omega_0+c\partial\phi/\partial\xi$. Photon density, frequency (5), frequency bandwidth (6), and pulse duration (7) are experimentally measurable quantities [20]. These markers of nonlinear optical processes make it possible to distinguish between the regimes of laser pulse propagation and wakefield excitation.

The transient stage of pulse propagation lasts for a couple of Rayleigh lengths. Fig. 2(e) shows that the pulse self-focuses near $x=0.35$ cm, increasing the intensity by approximately a factor of 2.5. It is during this stage that the expanding bubble self-injects electrons. Fig. 2(d) indicates that the mean pulse length (7) drops through the focusing stage, reaching the minimum near $x=0.6$ cm. Fig. 4(a) reveals that the reduction in central frequency and the bandwidth increase are only 10% at this point, which rules out strong longitudinal distortion associated with the negative GVD of the plasma. This reduction in $\langle\Delta\tau\rangle$ is thus a purely transverse effect associated with the stronger focusing of the most intense central part of the pulse.

After the focus, the pulse propagates rather uneventfully through $x=1.5$ cm. The average frequency steadily drops, the bandwidth grows, and stable self-guiding, accompanied by steady self-compression, begins near $x=0.8$ cm, at which point $\langle\Delta\omega\rangle$ is nearly 3 times its initial value. The pulse fully compresses at $x=1.45$ cm, at which point the instant frequency $\omega(\xi)$ is almost constant across the pulse body [cf. Fig. 4(b.2)]. This means that the pulse has reached the transform-limited duration permitted by the local bandwidth $\langle\Delta\omega(x)\rangle$. From Fig. 2 (d), this duration is $\langle\Delta\tau\rangle\approx 14$ fs, whereas the FWHM in intensity is half this value [cf. Fig. 4(b.2)]. Fig. 4(b.2) indicates that self-compression is quite symmetric with respect to the pulse centroid, which is strikingly different from the front etching and optical shock formation of the high-density regimes, $n_0>5\times10^{18}$ cm^{-3} [15–17]. The low-density plasma mitigates longitudinal deformations of the pulse. Indeed, variation of the nonlinear susceptibility at the pulse front is proportional to n_0. Nonlinear index perturbations, created by the pulse, have thus much lower contrast at low densities, resulting in much slower accumulation of the frequency red-shift. A drop of 30% in $\langle\omega\rangle$, requires 1.5 cm of propagation at the density $n_0=8.62\times10^{17}$ cm^{-3}, while only 0.7 mm at $n_0=1.3\times10^{19}$ cm^{-3} [17]. Moreover, an ultrashort pulse ($\omega_p\langle\Delta\tau\rangle<1$) of moderate amplitude ($|a(x)|\approx3.5$) does not maintain full blowout: electron density behind the driver always stays higher than 20% of the background. The red-shifted photons thus keep slipping towards the pulse tail. A strong intensity buildup is thus prevented, the positive outcome of which is complete insensitivity of the bubble size to the longitudinal deformations of the driver, the absence of continuous injection, and identically zero low-energy background in the electron spectra. It will be further explored in Section 3.2.

It appears that pulse front-etching arguments [7] do not strictly limit the acceleration length. Reaching the theoretical depletion point, $x=1.5$ cm, pulse still retains 70% of its energy. From this point on, the pulse evolution becomes rather unusual, with strongly asymmetric compression, previously reported for a similar density range in Refs. [18–20]. Fig. 3(c) and (d) indicates that the optical shock builds up in the pulse tail as the red-shifted photons accumulate. The shock amplitude, however, is weakly relativistic, and gradually diminishes as the pulse propagates further. The slippage of red photons through the pulse produces noticeable negative chirp evident in Fig. 4(c.2) and (d.2), and also leads to the steady growth of $\langle\Delta\tau\rangle$ [cf. Fig. 2(d)]. As a result, the pulse acquires a triangular shape [cf. Fig. 4(c.1)] with a steep tail and slowly rising front that subsequently diffracts, as is seen in progression from Fig. 3(b)–(d). This pulse shape leads to inefficient wake excitation, and accelerations halt after $x=2$ cm. Pulse depletion at this point is slightly above 50%.

3.2. *Electron self-injection and background-free acceleration*

The fully-3D PIC code CALDER-Circ [21] uses poloidal mode decomposition for the electromagnetic fields and currents, while computing macroparticle trajectories in the 3D Cartesian space. With our choice of initial conditions, using the two lowest-order

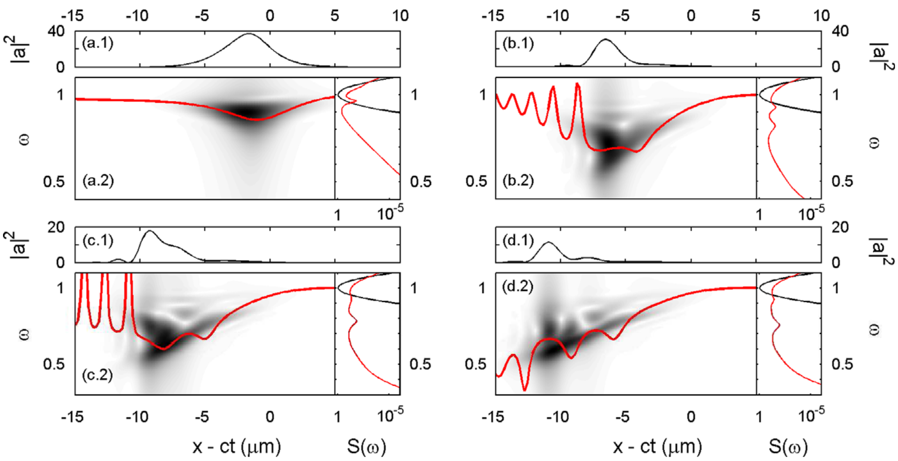

Fig. 4. Local frequency shifts and longitudinal amplitude deformations of the pulse in the course of its propagation. Panels (a), (b), (c), and (d) correspond to $x=0.6$, 1.45, 1.8, and 2.1 cm (as in Fig. 3) respectively. The pulse propagates from left to right. Panels (a.1)–(d.1) show the normalized intensity profile on axis. Panels (a.2)–(d.2) show the absolute value of the Wigner transform (grayscale) and the local frequency shift (in units of ω_0) extracted from the phase of the complex pulse envelope [red (gray) curves]. Insets show the radially integrated normalized spectral power $S(\omega)=\int_0^\infty \omega^2|a(x,r,\omega)|^2 r\,dr$ [black for the incident pulse and red (gray) corresponding to the given location x.] Panels (b.1) and (b.2) indicate that the pulse if fully compressed at $x=1.45$ cm: the frequency profile $\omega(\xi)$ is almost flat across the body of the pulse. As pulse propagates from $x=1.45$ to 2.1 cm, the red-shifted components slide through the pulse, imparting a negative frequency chirp and building up an optical shock at the rear. The intensity of the shock, is however, gradually decreasing, and the RMS pulse length [cf. Fig. 2(d)] is constantly increasing. The spectral energy density, $S(\omega)$, does not show noticeable changes through this process, which agrees with the mean frequency and frequency bandwidth remaining almost constant after $x=1.4$ cm [cf. Fig. 2(b) and (c)]. (WAKE simulation).

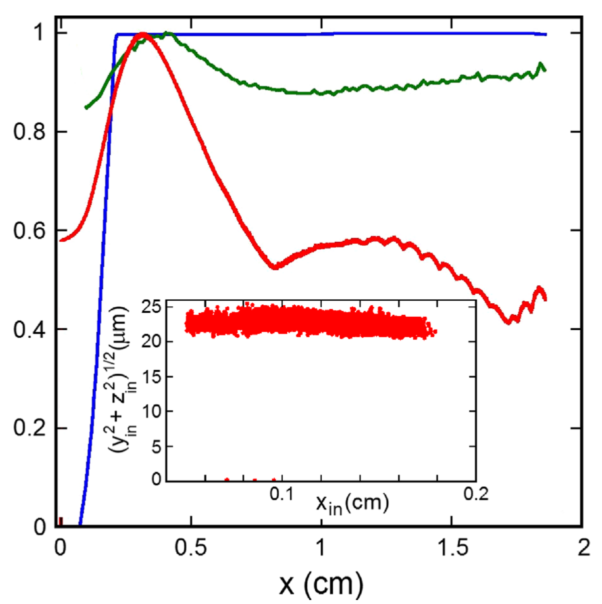

Fig. 5. Evolution of the laser pulse peak amplitude a [red (gray)], injected charge Q [blue (dark gray)], and the length of the rear half the bubble L_b [green (light gray)]. L_b is defined as the length of the accelerating phase on axis (the interval of negative electric field inside the bubble). All quantities are normalized to their respective global maximum values: $Q_{max}=0.43$ nC, $L_{b\ max}=29.2$ μm, and $a_{max}=7.36$. Inset: initial positions of self-injected electrons. (CALDER-Circ simulation).

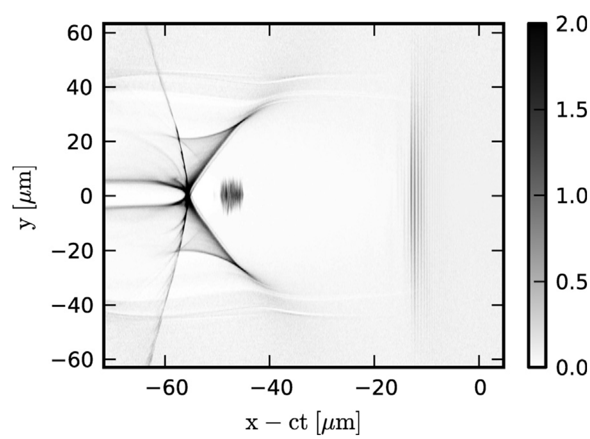

Fig. 6. Electron density in the laser polarization plane (in units of 10^{19} cm^{-3}), $x=1.86$ cm (CALDER-Circ simulation).

modes is sufficient to accurately capture the most important aspects of the interaction [9,27]. The simulation uses the longitudinal grid resolution $\Delta x=0.125c/\omega_0\approx 16$ nm, radial grid resolution $\Delta y=12\Delta x$, 50 macroparticles per cylindrical cell, a time step $\Delta t=0.124\omega_0^{-1}$, and propagates the laser pulse through $x=1.86$ cm.

The CALDER-Circ results yield a complete kinetic description of the accelerator dynamics predicted in WAKE simulation with test particles. Fig. 5 shows, in full quantitative agreement with Fig. 2(e) (WAKE simulation), that the laser pulse focuses upon entering the plasma, reaching peak amplitude at $x\approx 0.35$ cm. As the pulse focuses, the bubble expands. The length of the accelerating phase on axis (the region of negative longitudinal electric field) grows through $x\approx 0.4$ cm, triggering electron injection. As the bubble stabilizes and contracts, injection permanently stops. The collection volume of accelerated electrons reaching $x=1.86$ cm is shown in the inset in Fig. 5. Initially, all these electrons had with the radial offsets slightly below the local spot size of the pulse, and were trapped during the period of pulse focusing and bubble expansion. There is no evidence of self-injection from the near-axis area. The bubble size varies little over the distance as pulse self-guiding ($x>0.6$ cm), showing remarkable insensitivity to the longitudinal deformation of the driver. This nearly frozen bubble traps no electrons, and the accelerated charge remains constant.

The electron density distribution in the laser polarization plane at the end of simulation ($x=1.86$ cm) is shown in Fig. 6. The electron bunch is clearly far from the longitudinal center of the bubble, and hence far from dephasing. Thus, there is a prospect of further energy gain in a longer plasma. Although this image gives the evidence of

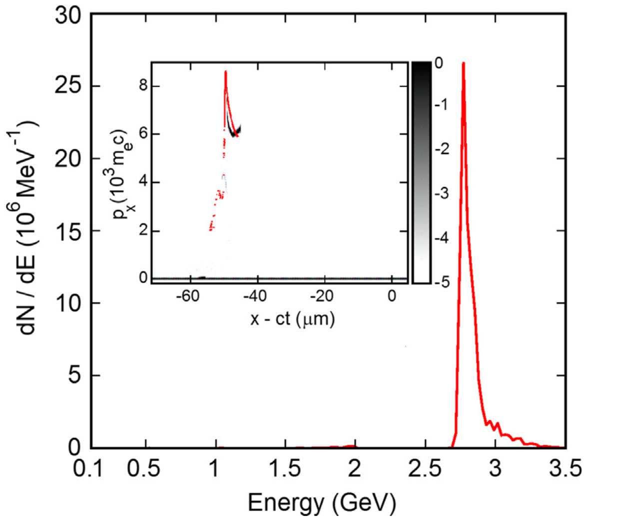

Fig. 7. Electron energy spectrum at $x = 1.86$ cm (CALDER-Circ simulation). Inset: longitudinal phase space of electrons reaching $x = 1.86$ cm. Grayscale shows the logarithm of the phase space density from the CALDER-Circ simulation. Red (gray) markers are the WAKE test particles.

pulse compression to roughly $2\lambda_0$ duration, the bubble remains remarkably axisymmetric. The pulse is apparently neither short enough nor relativistic enough to allow bubble shape distortion due to the carrier-envelope phase effects [15,16,28].

Fig. 7 shows the electron energy spectrum and longitudinal phase space at the end of the acceleration. The spectral peak has the average energy of 2.85 GeV, 4.3% RMS spread, and no noticeable low-energy background. The pulse central energy is fairly close to the estimate $\mathcal{E}+$ derived in Section 2 from the considerations of depletion-limited propagation. This background-free electron beam has total charge 0.43 nC, RMS spot size 3.57 μm, 4.9 mrad divergence, and the normalized transverse emittance $\varepsilon_\perp^N = 98$ mm mrad, where $\varepsilon_\perp^N = [(\varepsilon_x^N)^2 + (\varepsilon_y^N)^2]^{1/2}$, and $\varepsilon_i^N = (m_e c)^{-1}[(\langle p_i^2\rangle - \langle p_i\rangle^2)(\langle r_i^2\rangle - \langle r_i\rangle^2) - (\langle p_i r_i\rangle - \langle r_i\rangle\langle p_i\rangle)^2]^{1/2}$. Theory of beam loading in the blowout regime [29] tells that the beam has a factor of 4.5 less charge than needed to fully load the bucket and disrupt acceleration. Thus, the bubble in Fig. 6 remains closed, and acceleration can possibly go beyond the depletion-limited estimate.

The density of CALDER-Circ macroparticles in longitudinal phase space (cf. Fig. 7) shows negligible traces of particles between the main beam and the background ($p_x = 0$). The predictive capability of WAKE for this acceleration regime is verified in Fig. 7 by direct comparison of the test electron distribution (red markers) with the CALDER-Circ macroparticle density. The similarity of the phase spaces and precise agreement on the low-energy cutoff after the long-distance propagation indicates that, in spite of the approximations, orders of magnitude larger mesh and time steps, and the absence of beam loading, the WAKE simulations have remarkable predictive capability for the whole system dynamics (except for the transverse phase space of the bunch [16]).

Finally, we find that by $x = 1.86$ cm the pulse deposits 8 J of its energy to the plasma, of which 1.22 J is transferred to the electron beam. A significant pulse depletion thus improves energy efficiency to almost 10%, which is much higher than any QME LPA experiments have shown to date. Realization of this regime at the CILEX facility should be a significant step forward in advanced acceleration methods.

4. Summary and outlook

The physical processes at work in sub-30 fs, PW laser-driven plasma accelerators are identified. Acceleration occurs in the blowout regime with electron self-injection and pulse self-guiding beyond the theoretical depletion limit. Maintaining the delicate balance between vacuum-like diffraction and a pulse collapse due to the relativistic self-focusing helps achieve sufficient flexibility in the parameters of the accelerated electrons. The range of parameters is established for production of QME, 100 pC-scale electron beams with the energy up to 3 GeV and identically zero low-energy background. To this effect, the density of uniform, sub-2 cm-length plasmas should stay within the range from $n_0 = 5 \times 10^{17}$ to 10^{18} cm^{-3}. The hallmarks of this optimal regime are (a) early transient evolution of the optical driver and the accelerating bucket that causes injection of ambient plasma electrons, and (b) subsequent transverse stabilization of the system that turns off injection for good, preserving absolute energy spread of injected bunch through the end of acceleration. At low plasma density, the frequency red-shift is greatly reduced, precluding rapid self-steepening of the pulse leading edge into a relativistic optical shock [15–17]. The shock forms instead in the pulse tail after propagation beyond the theoretical depletion limit, thus having little effect on the wakefield. The phase space volume of the electron bunch thus remains low through the entire acceleration process.

The simulation results show that acceleration extends well beyond the theoretical pulse depletion limit. Pulse quality degradation eventually limits wake excitation, thus preventing electrons from reaching dephasing and limiting their energy to 3 GeV. At this limit, the relative energy spread drops below 5%. With nearly 10% of pulse energy transferred to the electron bunch, the acceleration process shows higher energy efficiency than any of the QME LPA experiments reported to date. This interaction regime is relevant to the upcoming experiments with the Apollon-10P CILEX laser whose goal is the production of nC-charge, background-free GeV electron beams for staged acceleration and radiation physics applications.

Acknowledgments

CALDER-Circ simulations of this work were performed using the PRACE Research Infrastructure resource Curie based in France at TGCC. The work of SYK and BAS is supported by the U.S. DOE Grant DE-SC0008382, NSF Grant PHY-1104683, and the U.S. DOD AFOSR Grant FA9550-11-1-0157.

References

[1] K. Nakamura, B. Nagler, Cs. Tóth, et al., Phys. Plasmas 14 (2007) 056708.
[2] S. Banerjee, N.D. Powers, V. Ramanathan, et al., Phys. Plasmas 19 (2012) 056703.
[3] H.T. Kim, K.H. Pae, H.J. Cha, et al., Phys. Rev. Lett. 111 (2013) 165002.
[4] M. Aoyama, K. Yamakawa, Y. Akahane, et al., Opt. Lett. 28 (2003) 1594.
[5] J.H. Sung, S.K. Lee, T.J. Yu, T.M. Jeong, J. Lee, Opt. Lett. 35 (2010) 3021.
[6] Ch. Liu, S. Banerjee, J. Zhang, et al., in: Proceedings of SPIE, vol. 8599, 2013, p. 859919. http://dx.doi.org/10.1117/12.2005008.
[7] W. Lu, M. Tzoufras, C. Joshi, et al., Phys. Rev. ST Accel. Beams 10 (2007) 061301.
[8] B. Cros, B.S. Paradkar, X. Davoine, et al., Laser plasma acceleration of electrons with multi-PW laser beams in the frame of CILEX, in this issue.
[9] S.Y. Kalmykov, S.A. Yi, A. Beck, et al., New J. Phys. 12 (2010) 045019.
[10] S.Y. Kalmykov, S.A. Yi, A. Beck, et al., Plasma Phys. Control. Fusion 53 (2011) 014006.
[11] S.Y. Kalmykov, A. Beck, S.A. Yi, et al., in: AIP Conference Proceedings, vol. 1299, 2010, pp. 174–179. http://dx.doi.org/10.1063/1.3520309.
[12] P. Mora, T.M. Antonsen Jr., Phys. Plasmas 4 (1997) 217.
[13] W. Zhu, J.P. Palastro, T.M. Antonsen Jr., Phys. Plasmas 19 (2012) 033105.
[14] W. Zhu, J.P. Palastro, T.M. Antonsen Jr., Phys. Plasmas 20 (2013) 073103.
[15] S.Y. Kalmykov, A. Beck, S.A. Yi, et al., Phys. Plasmas 18 (2011) 056704.
[16] S.Y. Kalmykov, A. Beck, X. Davoine, E. Lefebvre, B.A. Shadwick, New J. Phys. 14 (2012) 033025.
[17] S.Y. Kalmykov, X. Davoine, B.A. Shadwick, All-optical control of electron self-injection in millimeter-scale, tapered dense plasmas, in this issue.
[18] D.F. Gordon, B. Hafizi, R.F. Hubbard, et al., Phys. Rev. Lett. 90 (2003) 215001.
[19] B.A. Shadwick, C.B. Schroeder, E. Esarey, Phys. Plasmas 16 (2009) 056704.

[20] J. Schreiber, C. Bellei, S.P.D. Mangles, et al., Phys. Rev. Lett. 105 (2010) 235003.
[21] A.F. Lifschitz, X. Davoine, E. Lefebvre, et al., J. Comput. Phys. 228 (2009) 1803.
[22] G.-Z. Sun, E. Ott, Y.C. Lee, P. Guzdar, Phys. Fluids 30 (1987) 526.
[23] P. Sprangle, E. Esarey, A. Ting, Phys. Rev. Lett. 64 (1990) 2011.
[24] P. Sprangle, E. Esarey, J. Krall, G. Joyce, Phys. Rev. Lett. 69 (1992) 2200.
[25] L.M. Gorbunov, S.Y. Kalmykov, P. Mora, Phys. Plasmas 12 (2005) 033101.
[26] S.Y. Kalmykov, L.M. Gorbunov, P. Mora, G. Shvets, Phys. Plasmas 13 (2006) 113102.
[27] B.M. Cowan, S.Y. Kalmykov, A. Beck, et al., J. Plasma Phys. 78 (2012) 469.
[28] E.N. Nerush, I.Yu. Kostyukov, Phys. Rev. Lett. 103 (2009) 035001.
[29] M. Tzoufras, W. Lu, F.S. Tsung, et al., Phys. Plasmas 16 (2009) 056705.